CERT1 mutations perturb human development by disrupting sphingolipid homeostasis

Charlotte Gehin,[1] Museer A. Lone,[2] Winston Lee,[3,4] Laura Capolupo,[1] Sylvia Ho,[1] Adekemi M. Adeyemi,[5] Erica H. Gerkes,[6] Alexander P.A. Stegmann,[7] Estrella López-Martín,[8] Eva Bermejo-Sánchez,[8] Beatriz Martínez-Delgado,[8] Christiane Zweier,[9,10] Cornelia Kraus,[9] Bernt Popp,[11,12] Vincent Strehlow,[11] Daniel Gräfe,[13] Ina Knerr,[14,15] Eppie R. Jones,[16] Stefano Zamuner,[17] Luciano A. Abriata,[18] Vidya Kunnathully,[19] Brandon E. Moeller,[20] Anthony Vocat,[1] Samuel Rommelaere,[21] Jean-Philippe Bocquete,[21] Evelyne Ruchti,[22] Greta Limoni,[22] Marine Van Campenhoudt,[22] Samuel Bourgeat,[22] Petra Henklein,[23] Christian Gilissen,[24,25] Bregje W. van Bon,[24] Rolph Pfundt,[24,25] Marjolein H. Willemsen,[24] Jolanda H. Schieving,[26] Emanuela Leonardi,[27,28] Fiorenza Soli,[29] Alessandra Murgia,[28] Hui Guo,[30] Qiumeng Zhang,[30] Kun Xia,[30] Christina R. Fagerberg,[31] Christoph P. Beier,[31] Martin J. Larsen,[31] Irene Valenzuela,[32] Paula Fernández-Álvarez,[32] Shiyi Xiong,[33] Robert Śmigiel,[34] Vanesa López-González,[35] Lluís Armengol,[36] Manuela Morleo,[37,38] Angelo Selicorni,[39] Annalaura Torella,[37,38] Moira Blyth,[40] Nicola S. Cooper,[41] Valerie Wilson,[42] Renske Oegema,[43] Yvan Herenger,[44] Aurore Garde,[45,46] Ange-Line Bruel,[46,47] Frederic Tran Mau-Them,[46,47] Alexis B.R. Maddocks,[48] Jennifer M. Bain,[49] Musadiq A. Bhat,[50] Gregory Costain,[51] Peter Kannu,[52] Ashish Marwaha,[5] Neena L. Champaigne,[53] Michael J. Friez,[53] Ellen B. Richardson,[53] Vykuntaraju K. Gowda,[54] Varunvenkat M. Srinivasan,[54] Yask Gupta,[55] Tze Y. Lim,[55] Simone Sanna-Cherchi,[55] Bruno Lemaitre,[21] Toshiyuki Yamaji,[56] Kentaro Hanada,[56] John E. Burke,[20,57] Ana Marjia Jakšić,[22] Brian D. McCabe,[22] Paolo De Los Rios,[1,17] Thorsten Hornemann,[2] Giovanni D'Angelo,[1,19,21] and Vincenzo A. Gennarino[3,58,59,60,61]

[1]Institute of Bioengineering (IBI), École Polytechnique Fédérale de Lausanne (EPFL), Lausanne, Switzerland. [2]Institute of Clinical Chemistry, University Hospital Zurich, University of Zurich, Zurich, Switzerland. [3]Department of Genetics and Development and [4]Department Ophthalmology, Columbia University Irving Medical Center, New York, New York, USA. [5]Department of Medical Genetics, Cumming School of Medicine, The University of Calgary, Calgary, Alberta, Canada. [6]University of Groningen, University Medical Center Groningen, Department of Genetics, Groningen, Netherlands. [7]Department of Clinical Genetics and School for Oncology and Developmental Biology (GROW), Maastricht University Medical Center, Maastricht, Netherlands. [8]Institute of Rare Diseases Research (IIER), Instituto de Salud Carlos III, Madrid, Spain. [9]Institute of Human Genetics, Friedrich-Alexander-Universität Erlangen-Nürnberg, Erlangen, Germany. [10]Department of Human Genetics, Inselspital, Bern University Hospital, University of Bern, Bern, Switzerland. [11]Institute of Human Genetics, University of Leipzig Medical Center, Leipzig, Germany. [12]Berlin Institute of Health at Charité – Universitätsmedizin Berlin, Center of Functional Genomics, Berlin, Germany. [13]Department of Pediatric Radiology, University Hospital Leipzig, Leipzig, Leipzig, Germany. [14]National Centre for Inherited Metabolic Disorders, Children's Health Ireland (CHI) at Temple Street, Dublin, Ireland. [15]UCD School of Medicine, Dublin, Ireland. [16]Genuity Science, Cherrywood Business Park, Dublin, Ireland. [17]Institute of Physics, School of Basic Sciences, École Polytechnique Féderale de Lausanne (EPFL), Lausanne, Switzerland. [18]Laboratory for Biomolecular Modeling and Protein Purification and Structure Facility, EPFL and Swiss Institute of Bioinformatics, Lausanne Switzerland. [19]Institute of Biochemistry and Cell Biology, National Research Council, Naples, Italy. [20]Department of Biochemistry and Microbiology, University of Victoria, Victoria, Canada. [21]Global Health Institute, School of Life Sciences and [22]Brain Mind Institute, School of Life Sciences, EPFL, Lausanne, Switzerland. [23]Berlin Institute of Health, Institut für Biochemie, Charité-Universitätsmedizin Berlin, Corporate Member of Freie Universität Berlin, Humboldt-Universität zu Berlin, Berlin, Germany. [24]Radboud University Medical Center, Department of Human Genetics, Nijmegen, Netherlands. [25]Radboud Institute for Molecular Life Sciences, Nijmegen, Netherlands. [26]Radboud University Medical Center, Department of Pediatric Neurology, Amalia Children's Hospital and Donders Institute for Brain, Cognition and Behavior, Nijmegen, Netherlands. [27]Molecular Genetics of Neurodevelopment, Department of Woman and Child Health, University of Padova, Padova, Italy. [28]Fondazione Istituto di Ricerca Pediatrica (IRP), Città della Speranza, Padova, Italy. [29]Medical Genetics Department, APSS Trento, Trento, Italy. [30]Center for Medical Genetics and Hunan Key Laboratory of Medical Genetics, School of Life Sciences, Central South University, Changsha, Hunan, China. [31]Department of Neurology, Odense University Hospital, and Department of Clinical Research, University of Southern Denmark, Odense, Denmark. [32]Department of Clinical and Molecular Genetics, University Hospital Vall d'Hebron, Medicine Genetics Group, Valle Hebron Research Institute, Barcelona, Spain. [33]Fetal Medicine Unit and Prenatal Diagnosis Center, Shanghai First Maternity and Infant Hospital, Tongji University School of Medicine, Shanghai, China. [34]Department of Family and Pediatric Nursing, Medical University, Wroclaw, Poland. [35]Sección de Genética Médica, Servicio de Pediatría, Hospital Clínico Universitario Virgen de la Arrixaca, IMIB-Arrixaca, CIBERER-ISCIII, Murcia, Spain. [36]Quantitative Genomic Medicine Laboratories, S.L., CSO & CEO, Esplugues del Llobregat, Barcelona, Catalunya, Spain. [37]Telethon Institute of Genetics and Medicine (TIGEM), Pozzuoli, Naples, Italy. [38]Department of Precision Medicine, University of Campania "Luigi Vanvitelli," Naples, Italy. [39]Department of Pediatrics, ASST Lariana Sant' Anna Hospital, San Fermo Della Battaglia, Como, Italy. [40]North of Scotland Regional Genetics Service, Clinical Genetics Centre, Ashgrove House, Foresterhill, Aberdeen, United Kingdom. [41]W Midlands Clinical Genetics Service, Birmingham Women's Hospital, Edgbaston Birmingham, United Kingdom. [42]Northern Regional Genetics Laboratory, Newcastle upon Tyne, United Kingdom. [43]Department of Genetics, University Medical Center Utrecht, Utrecht University, Utrecht, Netherlands. [44]Genetica AG, Humangenetisches Labor und Beratungsstelle, Zürich, Switzerland. [45]Centre de Référence Anomalies du Développement et Syndromes Malformatifs, FHU TRANSLAD, Hôpital d'Enfants, CHU Dijon, Dijon, France. [46]UMR1231 GAD, INSERM – Université Bourgogne-Franche Comté, Dijon, France. [47]Unité Fonctionnelle Innovation en Diagnostic Génomique des Maladies Rares, FHU-TRANSLAD, CHU Dijon Bourgogne, Dijon, France. [48]Department of Radiology at Columbia University Irving Medical Center, New York, New York, USA. [49]Department of Neurology, Columbia University Irving Medical Center, New York Presbyterian Hospital, Columbia University Medical Center, New York, New York, USA. [50]Institute of Pharmacology and Toxicology University of Zürich, Zürich, Switzerland. [51]Division of Clinical and Metabolic Genetics, The Hospital for Sick Children, Toronto, Ontario, Canada. [52]Department of Medical Genetics, University of Alberta, Edmonton, Alberta, Canada. [53]Greenwood Genetic Center and the Medical University of South Carolina, Greenwood, South Carolina, USA. [54]Department of Pediatric Neurology, Indira Gandhi Institute of Child Health, Bangalore, India. [55]Division of Nephrology, Department of Medicine, Columbia University, New York, New York, USA. [56]Department of Biochemistry and Cell Biology, National Institute of Infectious Diseases, Tokyo, Japan. [57]Department of Biochemistry and Molecular Biology, The University of British Columbia, Vancouver, British Columbia, Canada. [58]Department of Pediatrics, [59]Department of Neurology, [60]Columbia Stem Cell Initiative, and [61]Initiative for Columbia Ataxia and Tremor, Columbia University Irving Medical Center, New York, New York, USA.

Neural differentiation, synaptic transmission, and action potential propagation depend on membrane sphingolipids, whose metabolism is tightly regulated. Mutations in the ceramide transporter CERT (*CERT1*), which is involved in sphingolipid biosynthesis, are associated with intellectual disability, but the pathogenic mechanism remains obscure. Here, we characterize 31 individuals with de novo missense variants in *CERT1*. Several variants fall into a previously uncharacterized dimeric helical domain that enables CERT homeostatic inactivation, without which sphingolipid production goes unchecked. The clinical severity reflects the degree to which CERT autoregulation is disrupted, and inhibiting CERT pharmacologically corrects morphological and motor abnormalities in a *Drosophila* model of the disease, which we call ceramide transporter (CerTra) syndrome. These findings uncover a central role for CERT autoregulation in the control of sphingolipid biosynthetic flux, provide unexpected insight into the structural organization of CERT, and suggest a possible therapeutic approach for patients with CerTra syndrome.

Introduction

Sphingolipids play numerous essential roles in membrane structure, signal transduction, and brain development and function (1–3). The central nervous system is particularly affected by disturbances in sphingolipid production or clearance: defective production can cause hereditary sensory neuropathy, spastic paraplegia, or infantile epilepsy syndrome, whereas toxic accumulation of sphingolipids underlies a number of devastating inborn errors of metabolism such as Gaucher disease, Farber disease, Niemann-Pick disease type A, Krabbe, Tay-Sachs, and Sandhoff diseases (1, 4). Sphingolipid metabolic fluxes therefore must be tightly regulated through homeostatic circuits (5). A key checkpoint in sphingolipid biosynthesis occurs at contact sites between the endoplasmic reticulum (ER) and the *trans* Golgi membrane, where the ceramide transporter (CERT) transfers ceramide (Cer) from the ER to the *trans* Golgi for its conversion to sphingomyelin (SM) (6). When sufficient rates of SM production are reached, CERT is phosphorylated and undergoes a conformational change that renders it inactive (7).

Given the central position of CERT in sphingolipid metabolism, its malfunction should be detrimental to human health and particularly to neural function. Thus far, 1 case report and several case-control screening studies have described associations between variants in ceramide transporter 1 (*CERT1*), the gene that encodes CERT, and neurological abnormalities (8–16). Nonetheless, there has not been a systematic assessment of the mutational landscape of *CERT1* in humans, and whether or how *CERT1* mutations cause neurological disease remains to be proven.

In this study, we characterized 31 unrelated individuals with 22 distinct missense variants in *CERT1*, 18 of which have not to our knowledge been previously reported. These patients have a syndromic presentation characterized by infantile hypotonia; mild dysmorphologies (affecting the face, hands or feet); variable degrees of intellectual disability and motor and speech delays; increased pain tolerance; and seizures. We investigated the effect of Cer transporter (CerTra) mutations on CERT function, regulation, and structure. We found that several CerTra mutations disrupt CERT autoregulation, leading to a gain in CERT activity, increased de novo sphingolipid synthesis in the ER, and skewed metabolic flux toward the production of potentially neurotoxic compounds. We found that CERT gain of function in *Drosophila melanogaster* led to head and brain size defects and impaired locomotor activity, which we corrected by pharmacological inhibition of CERT. Biochemical characterization of disease-causing *CERT1* mutations led us to identify an unanticipated structured region within CERT that is essential to its autoregulation and to sphingolipid homeostasis.

Results

Characterization of CERT1-associated phenotypes

Most of the *CERT1* variants reported so far have been associated with intellectual disability (13) (Figure 1A, and Supplemental Table 1; supplemental material available online with this article; https://doi.org/10.1172/JCI165019DS1), but the clinical phenotype has been characterized for only 1 of these individuals, who carries a p.S135P variant (13). We therefore sought *CERT1* mutation carriers from multiple international disease consortia and databases (see Methods and Supplemental Methods). We identified 50 patients who carry a potentially pathogenic variant in *CERT1* (45 in the coding sequence; hg19:NM_005713.3, Figure 1A, and Supplemental Tables 1 and 2) (17). We obtained thorough clinical histories for 31 patients: 27 from the present cohort, 3 who were initially included in genetic screening consortia for intellectual disability (8, 10, 12), and the patient who had been characterized clinically (13) (Supplemental Tables 2 and 3, and Supplemental Clinical Appendix for each patient). Family segregation confirmed that *CERT1* variants occurred de novo in 93% (25 of 27) of patients. Biparental samples were not available for 4 of the patients (referred to herein as subject 1 [S1], S19, S20, and S24; see Supplemental Clinical Appendix). The p.V326F variant in S21 was inherited from her reportedly unaffected father, whereas the p.A449V variant in S26 was inherited from her mother, who was diagnosed with intellectual disability (Supplemental Table 2 and Supplemental Clinical Appendix).

The detailed clinical information we were able to gather (see Supplemental Clinical Appendix and Supplemental Table 2)

Authorship note: CG, MAL, WL, and LC contributed equally to this work. TH, GDA, and VAG co-supervised this work.
Conflict of interest: The authors have declared that no conflict of interest exists.

Submitted: August 31, 2022; **Accepted:** March 22, 2023; **Published:** May 15, 2023.
Reference information: *J Clin Invest*. 2023;133(10):e165019.
https://doi.org/10.1172/JCI165019.

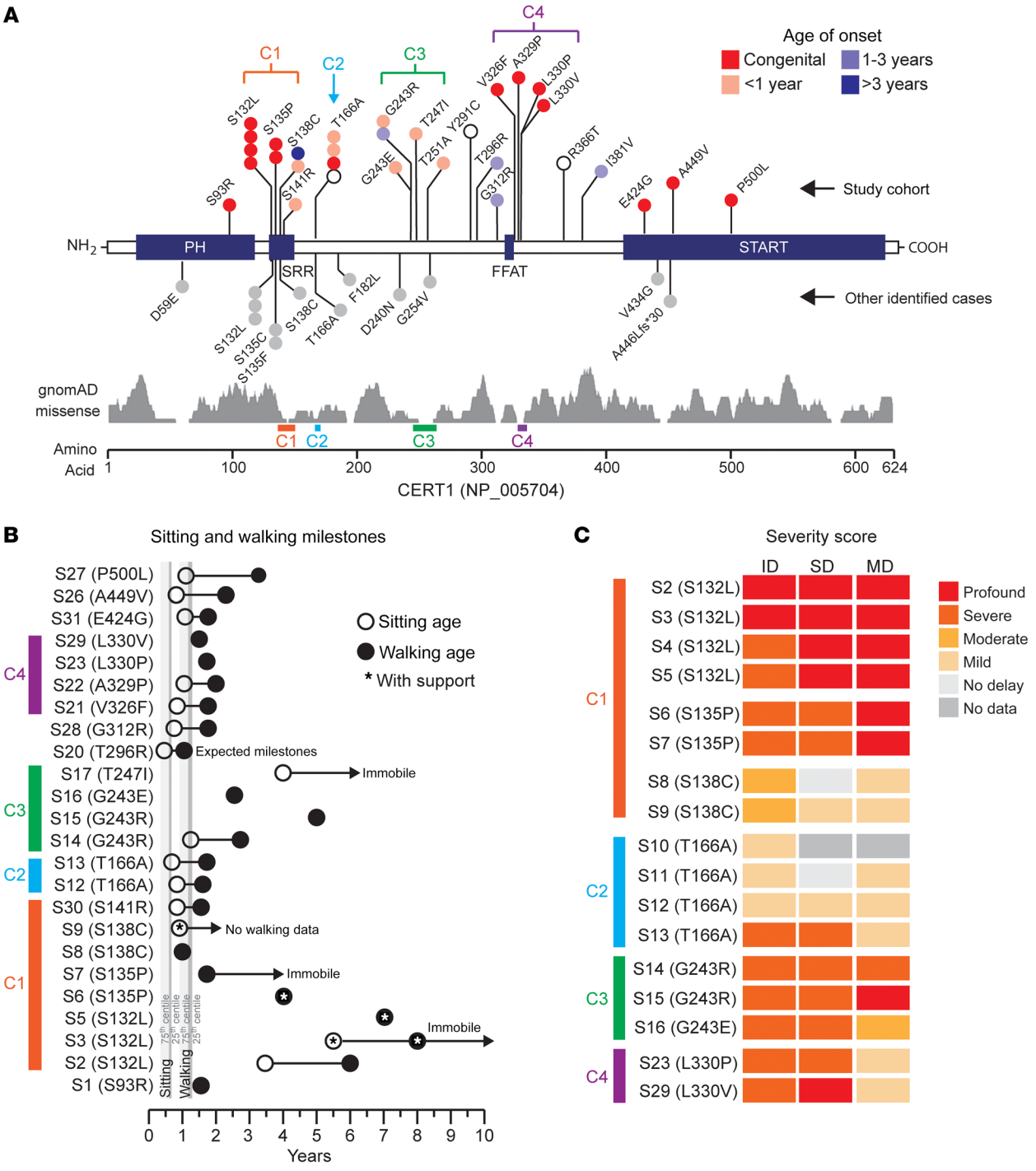

Figure 1. Mutations in *CERT1* lead to a neurodevelopmental syndrome. (**A**) Schematic representation of functional domains in CERT. The N-terminal PH domain interacts with phosphoinositide phosphatidylinositol-4-phosphate [PtdIns(4)*P*] (25) on the *trans* Golgi. The SRR is the target of protein kinase D (PKD) and casein kinase 1γ2 (CSNK1G2) phosphorylation. The FFAT (2 phenylalanines in an acidic tract) motif interacts with the integral membrane proteins VAP-A and VAP-B on the ER (70), and a C-terminal START-related domain extracts Cer from the ER membrane and delivers it to the *trans* Golgi (7). The schematic shows coding variants in *CERT1* (NP_005704) in our cohort of 31 individuals above the gene diagram and other individuals identified from clinical databases (DECIPHER, version 9.31, ClinVar, and VKGL) below it (Supplemental Table 1). Colors indicate the age of onset; gray indicates that no information is available. The distribution of gnomAD singleton missense variants for healthy individuals is plotted below. (**B**) Range of severity in motor delays compared with the 75th percentile (light gray) and 25th percentile (dark gray), adapted from values published by the Denver Developmental Screening Test II. White and black circles indicate delayed sitting and walking ages, respectively; asterisks indicate that the individual needs sitting or walking support. White circles with an arrow indicate individuals who are currently immobile or have not yet developed independent walking. (**C**) Heatmap shows the degree of intellectual disability (ID), speech delay (SD), and motor delay (MD) of the patients bearing frequent *CERT1* mutations. See Supplemental Table 2 for scores. C1, cluster 1; C2, cluster 2; C3, cluster 3; C4, cluster 4.

Table 1. Phenotype-genotype correlations for variants for which there was more than 1 study participant

Variant	Key features
S132L (*n* = 4, S2-S5)	Small at birth, perinatal difficulties, failure to thrive. Achieve sitting at 3–4 yr of age; may walk, supported, by 7 or 8 yr of age but may become immobile by late adolescence. Seizures severe enough to require hospitalization. Profound to severe ID.
S135P (*n* = 2, S6-S7)	Somewhat small at birth, perinatal difficulties, failure to thrive. Achieve sitting between 19 mo and 4 yr of age. Seizures may occur after infancy. Severe ID.
S138C (*n* = 2, S8-S9)	Normal to slightly low birth weight, may have feeding difficulties. Mild motor delay (may sit at 10 mo), mild speech delay. No seizures. Moderate ID.
T166A (*n* = 4, S10-S13)	Normal birth weight. Mild motor delay at 1 year of age, mild speech delay (can use complete sentences at 5 years). Seizures likely. May have moderate, mild, or no notable ID. Exception: Patient 13 has severe epileptic encephalopathy and severe ID.
G243R (*n* = 2, S14-S15)	Normal birth weight, no neonatal difficulties, but 1 patient was noted to have developmental delay by the age of 4 mo (patient 14). Acquired growth delay; development slows or regresses, may become nonverbal. Seizures. Severe ID.

Although it is difficult to draw firm conclusions from 2 to 4 patients, we can sketch the main features that are associated with each variant thus far on the basis of available information. See the Clinical Appendix and Supplemental Table 2 for details on all 31 patients.

revealed cognitive, motor, and speech delays of variable degrees of severity. Of the patients for whom we had birth information, only 4 were of average weight at birth; most were born slightly to significantly underweight. Similarly, only 4 of the individuals did not show some form of developmental delay by the end of the first year of life (4 of 26, 15%), with the latest onset being at age 4 years (Figure 1, A–C). Fifteen (of 24) patients had neonatal feeding difficulties, often with hypotonia or failure to thrive. These were likely early manifestations of what would later become frank motor delays, affecting 26 of 29 patients (Figure 1B). Intellectual disability ranged from mild to profound, as per the criteria of the Diagnostic and Statistical Manual of Mental Disorders, 5th Edition (DSM-5) (18) (see Methods); the latter individuals are nonverbal, lack age-appropriate daily living skills, and require safety supervision. Neurobehavioral abnormalities frequently led to a diagnosis of autism spectrum disorder (ASD) (19 of 27, 70%); some patients displayed stereotypical hand movements (14 of 18), self-injurious behavior (9 of 19), high pain tolerance (9 of 18), disrupted sleep patterns (9 of 21), attention deficit–hyperactivity disorder (10 of 19), or aggression (6 of 20). Multiple seizure types were reported (16 of 29). Neuroimaging frequently revealed a thin corpus callosum, ventriculomegaly, delayed myelination, and cerebellar atrophy (Supplemental Figure 1B).

Subtle facial dysmorphisms included anteverted nares with a depressed or broad nasal bridge, enlarged earlobes, synophrys, micrognathia, dental anomalies (protruding incisors and diastema), and palatine ridges (Supplemental Figure 1A and Supplemental Figure 2, A–E). Anomalies affecting the hands, feet, or digits included third/fourth finger syndactyly, club foot, or hallux varus (sandal gaps); the first metatarsal also tended to be short, whereas the fifth fingers tended to be long (Supplemental Figure 2F).

The majority (27 of 31, 87%) of variants from our enrolled patients occurred in the region between the pleckstrin homology (PH) and C-terminal START-related (START) domain (Figure 1A), as was the case for previously reported variants (13). These variants populated 4 distinct subregions, whereby the geometric mean distance (δg) between variants within each spatial group indicated a greater likelihood of clustering compared with random permutations (Figure 1A). Human *CERT1* produces at least 2 splicing variants that are both widely expressed (13). In this report, we have used *CERT1* isoform 1 (also known as $CERT_L$) for both aa numbering, overexpression, and structural experiments.

The first 4 serine residues of the serine-rich region (SRR) (132-SMVSLVSGASGYSATSTSS-150) are hotspots for mutations (cluster 1): p.S132 (*n* = 7; 4 enrolled), p.S135 (*n* = 4; 2 enrolled), p.S138 (*n* = 4; 2 enrolled), p.S141 (*n* = 1; 1 enrolled) (Figure 1A). An alanine substitution at p.T166 was found in 5 study participants in our cohort (4 enrolled; cluster 2). Between residues 240 and 254 (cluster 3), missense variants were found at p.D240 (*n* = 1), p.G243 (*n* = 4; 4 enrolled), p.T247 (*n* = 1; 1 enrolled), and p.T251 (*n* = 1; 1 enrolled). Four variants, p.V326F, p.A329P, p.L330V, and p.L330P, are located at the C-terminal end of the CERT FFAT motif (cluster 4).

For the variants that recurred in multiple individuals, we were able to sketch out broad genotype-phenotype correlations. The most severe phenotypes — with congenital or perinatal onset, profound-to-severe intellectual disability, and the greatest motor delay — resulted from mutations at p.S132 and p.S135 (Figure 1, B and C, and Table 1). Individuals bearing mutations at p.S138, p.T166, or p.G243 tended to not have perinatal difficulties and achieved early developmental milestones (S8 did not show difficulties until 4 years of age) but then regressed or slowed in their development. Seizures probably contribute to the developmental delays: neither individual with a p.S138C mutation had seizures and have only moderate intellectual disability, but S13, the most severely affected of the p.T166A carriers, has an epileptic encephalopathy that apparently halted her development at 19 months of age. All variants associated with more severe phenotypes were predicted to be deleterious by Combined Annotation-Dependent Depletion, version 1.6 (CADD v1.6), Rare Exome Variant Ensemble Learner (REVEL), Mendelian Clinically Applicable Pathogenicity (M-CAP), and Eigen (Supplemental Table 4). Approximately half of the variants among the more moderately affected individuals had inconsistent pathogenicity predictions across algorithms. On average, variants among patients had significantly greater CADD v1.6, M-CAP, REVEL, and Eigen pathogenicity scores than did Genome Aggregation Database (gnomAD) singleton missense variants ($P < 0.001$, Mann-Whitney *U* test).

Variants p.D59E (15), p.T166A (19), and p.F182L (9) were previously identified in ASD cohorts (Supplemental Table 1). To determine the extent to which *CERT1* mutations contribute to autism,

we conducted a targeted de novo analysis interrogating the Simons Foundation Powering Autism Research (SPARK) initiative database, which includes genomic data from nearly 35,000 individuals with ASD (See Supplemental Methods). No de novo protein-altering variants were observed in the Simons exome cohort. Denovo-db (version 1.6.1) confirmed the negative findings for the exome cohort but identified 1 de novo genome missense mutation (pos=74721285, T>C, c.880A>G, p.(T294A), exon6) in 1 of 516 trios. This analysis, along with the fact that none of the individuals in our cohort was diagnosed with ASD as a primary condition, indicates that *CERT1* variants are unlikely to be a significant contributor to autism but instead cause a recognizable neurodevelopmental syndrome distinct from ASD, which we will refer to as CerTra syndrome.

CerTra mutations disrupt CERT regulation

CERT oscillates between cytosolic and membrane-associated forms (20), according to its activation state in the homeostatic cycle (7). Active, membrane-associated CERT provides Cer to SM synthase 1 (SMS1) for its conversion to SM, with concomitant production of diacylglycerol. The diacylglycerol produced in the SM synthase 1 reaction triggers a signaling response involving the recruitment of protein kinase D (PKD) to the *trans* Golgi (21–23). PKD initiates CERT phosphorylation at p.S132 (7); and CSNK1G2 (casein kinase 1 γ 1) then phosphorylates the rest of the SRR phosphosites (24–27). Following phosphorylation, CERT undergoes a conformational change that leads to its cytosolic redistribution and inactivation (20, 26, 28); all this can then be reversed by the action of the ER phosphatase PP2Cε (protein phosphatase 2C epsilon) (29). Mutations leading to abnormally activated CERT redistribute the protein to Golgi membranes and cytosolic spots, while inactivating mutations redistribute it to the cytosol (30, 31).

To determine whether disease-causing variants alter CERT localization, we used automated microscopy to capture GFP-tagged WT and CerTra-associated CERT variants in transfected HeLa cells (see Supplemental Methods). Eighteen of the 22 CERT mutants exhibited a greater tendency than WT to associate with the perinuclear membranes and cytosolic spots (Figure 2, A and B). These included all variants mapping to clusters 1 to 4 (Figure 1A), those located between clusters 3 and 4, the p.S93R in the PH domain, and the p.500L in the START domain. We observed a similar phenotype in patient-derived fibroblasts bearing the p.G243R mutation (Supplemental Figure 3, A–C). Four consecutive variants (p.R366T, p.I382V, p.E424G, p.A449V) did not show a different distribution compared with CERT WT.

We next evaluated the phosphorylation pattern of CERT WT and mutants by SDS-PAGE (Figure 2C). WT CERT migrates on SDS gels as a doublet, with the fast- and slow-migrating bands corresponding to the active/hypophosphorylated and the inactive/hyperphosphorylated forms of CERT, respectively (24). By contrast, all variants belonging to clusters 1, 2, and 3 showed hypophosphorylation, whereas mutations outside of these clusters did not. Mass spectrometry–based assessment of selected variants belonging to clusters 1, 2, and 3 showed that these *CERT1* mutations did not affect CERT phosphorylation outside the SRR or SRR monophosphorylation (likely on p.S132), and suggests that CSNK1G2-mediated SSR phosphorylation is defective in these mutants (Supplemental Figure 3D).

Although we expected hypophosphorylation and increased membrane recruitment for CERT mutants within the SRR (cluster 1) (13, 27), this was not intuitive for clusters 2 and 3. We therefore investigated the regulation of the 2 most frequent *CERT1* mutations in these clusters, p.G243R, for which some biochemical characterization was already reported (30), and p.T166A. These 2 variants were effectively phosphorylated at p.S132 by PKD in both in vitro and cell-based assays (Supplemental Figure 3, D and E). Moreover, the p.S132 phosphomimetic mutant (HGS 130-132 DDD) (27) in the p.G243R and p.T166A backgrounds did not differ in either localization or SDS-PAGE migration (Supplemental Figure 3, F–H). This supports the idea that the cluster 2 and 3 mutations affect CERT regulation downstream of PKD phosphorylation. To test this possibility, we coexpressed CSNK1G2 or PP2Cε with the hypophosphorylated CERT mutants. Overexpression of CSNK1G2 led to reduced membrane association of most mutants (p.S132L served as a negative control) (Figure 3, A–C), indicating that these can be phosphorylated and inactivated by CSNK1G2. Interestingly, although PP2Cε overexpression had little effect on WT CERT phosphorylation or localization, consistent with previous results (27), hypophosphorylated CERT mutants were sensitive to PP2Cε overexpression (Figure 3, A–C).

Thus, CerTra-associated *CERT1* mutations generally disturb CERT regulation and promote its membrane association. Mutations in clusters 1, 2, and 3 also reduce the pool of hyperphosphorylated/inactive CERT by influencing the CERT phosphorylation cycle that depends on the consecutive action of PKD and CSNK1G2 kinases and on the PP2Cε phosphatase.

CerTra mutations disrupt sphingolipid homeostasis

Sphingolipid biosynthesis starts at the ER with the generation of Cer (32–34). Cer is then transported to the Golgi complex by vesicular carriers for the production of glucosylceramide and downstream glycosphingolipids, or transferred directly to the *trans* Golgi by CERT for its conversion to SM (6) (Figure 4A).

We profiled sphingolipids in *CERT1*-deficient (*CERT1*-KO) HeLa cells expressing 6 CERT mutants tagged with GFP. *CERT1* KO causes a defect in Cer-to-SM conversion (35) that is expected to be reverted by the expression of active CERT. Overexpression of WT CERT in *CERT1*-KO cells, in fact, induced a 5-fold increase in SM levels coupled with an unexpected increase in Cer and complex glycosphingolipids (Figure 4B and Supplemental Figure 4A). Overexpression of CERT mutants also increased SM and Cer levels but markedly reduced glycosphingolipid levels compared with WT levels. Unexpectedly, CERT overexpression increased dihydroceramide (dhCer) and dihydrosphingomyelin (dhSM), and this was even more pronounced with mutant overexpression (Figure 4B and Supplemental Figure 4A). Variants associated with more severe manifestations in patients (i.e., at p.S132, p.S135, and p.G243) were associated with the greatest increases.

We observed that *CERT1* overexpression produced an overall increase in sphingolipid levels (Figure 4B). To determine whether this was due to increased synthesis, decreased catabolism, or both, we used a D_3-^{15}N-serine labeling approach (see Methods). Lipids were extracted and subjected to chemical hydrolysis to release long-chain bases (LCBs) from sphingolipids and dihydrosphingolipids. These LCBs reflect total levels of steady-state

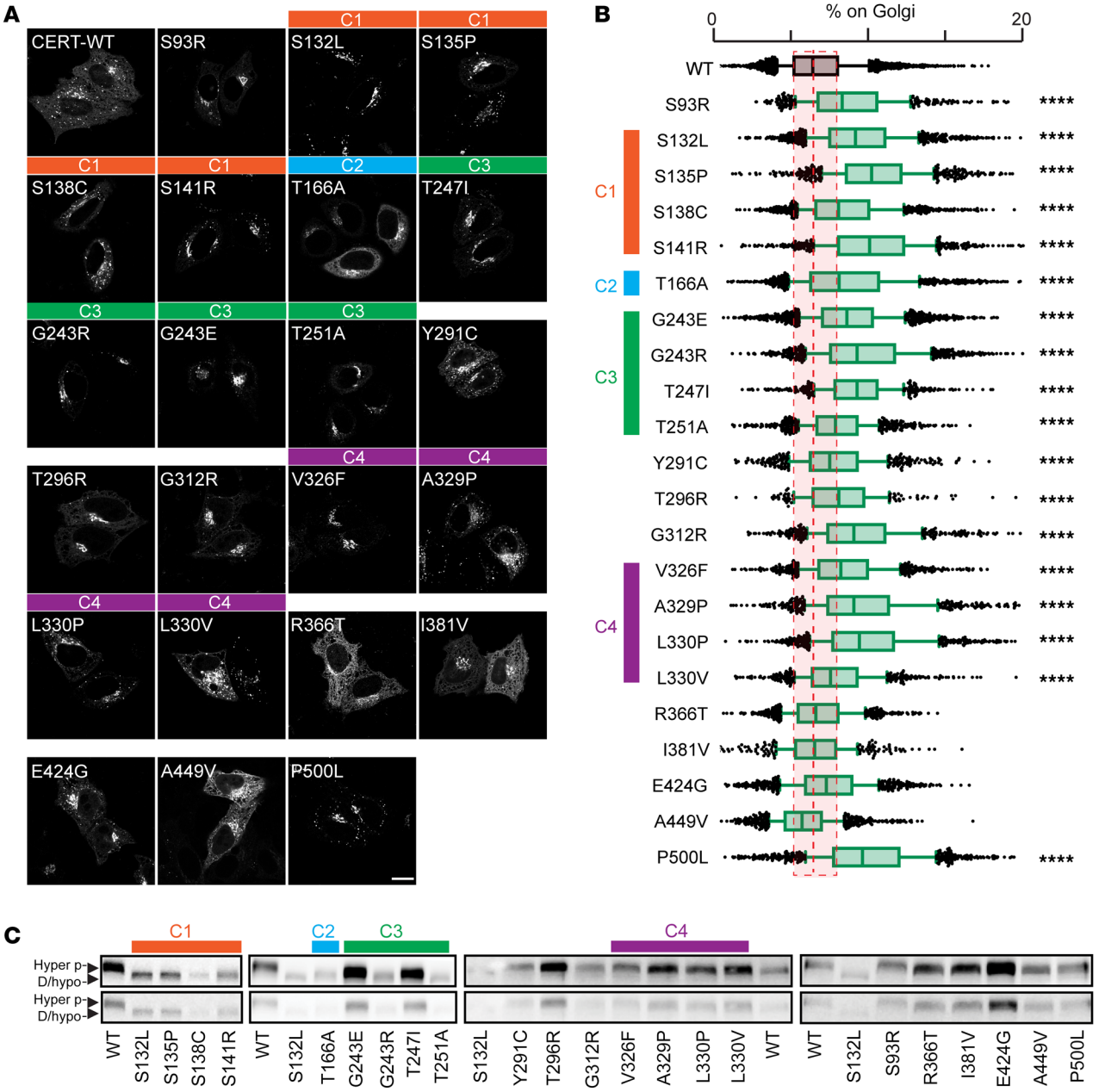

Figure 2. Disease-causing variants result in CERT misregulation. (**A**) CERT-GFP WT and mutant localization in HeLa cells analyzed by confocal microscopy. Scale bar: 20 μm. (**B**) Percentage of CERT-GFP WT and mutants associated with the Golgi complex in HeLa cells. Cells were stained with Hoechst and anti-GM130 antibody and analyzed by automated fluorescence microscopy (n >1,000 cells per condition; ****P < 0.0001, 1-way ANOVA, effect size >15%). WT CERT is shown in gray, and CerTra mutants are shown in green. Data are shown as box-and-whisker plots. Bars represent the median value of each data set. (**C**) Western blot of HeLa cells expressing CERT-GFP WT or mutants (n = 3). Hyperphosphorylated (Hyper p-) and de-/hypophosphorylated (D/hypo-) bands are indicated by arrowheads. The clusters, as in Figure 1, are indicated throughout **A**–**C**.

and newly synthesized sphingolipids, represented by sphingosine (SO) and sphingosine+3 (SO+3), respectively, while steady-state and newly synthesized dihydrosphingolipids are represented by sphinganine (SA) and sphinganine+3 (SA+3), respectively. Overexpression of CERT mutants had little effect on SO but increased SO+3 by 200%. All mutants had twice the amount of SA compared with WT CERT, but SA+3 levels rose at least 300% in the case of the mildest mutant, p.T166A, and considerably more for the other mutants (Figure 4C).

These data indicate that CERT activity promotes de novo sphingolipid production, possibly by relaxing the Cer-dependent inhibition of serine palmitoyltransferase (SPT) (36) (Supplemental Figure 5A). To test this hypothesis, we repeated our metabolic labeling experiment in parental and *CERT1*-KO HeLa cells treated with the CERT inhibitor *N*-[(1R,3S)-3-hydroxy-1-(hydroxymethyl)-3-phenylpropyl]-dodecanamide (HPA-12) (37) or, as a control, with myriocin (Myr), an inhibitor of SPT and therefore of sphingolipid production (Supplemental Figure 4A). Treatment with HPA-

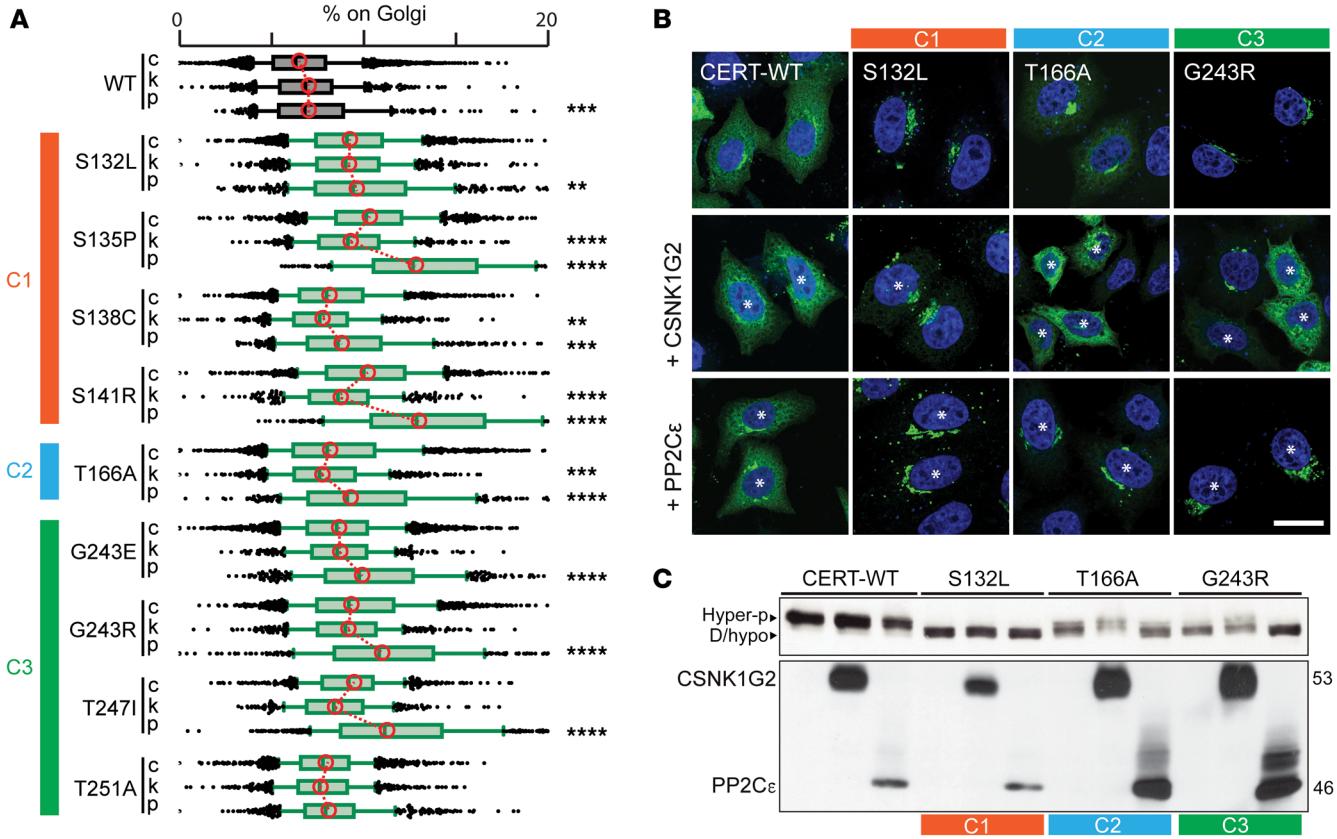

Figure 3. Disease-causing CERT variants are susceptible to phosphoregulation. (**A**) Percentage of CERT-GFP WT and mutants from clusters 1, 2, and 3 associated with the Golgi complex in HeLa cells overexpressing CSNK1G2-HA (k) or PP2Cε-HA (p). Cells were stained with Hoechst, anti-GM130 antibody, and anti-HA antibody and analyzed by automated fluorescence microscopy (n >500 cells per condition; $^{**}P < 0.01$, $^{***}P < 0.001$, and $^{****}P < 0.0001$, 1-way ANOVA). Bars represent the median value of each data set. (**B**) Subcellular localization of CERT-GFP WT, p.S132L, p.T166A, and p.G243R in HeLa cells expressing PP2Cε-HA or CSNK1G-HA. Cells were stained with DAPI (blue) and anti-HA antibody and analyzed by confocal microscopy. Asterisks indicate cotransfected cells. Scale bar: 20 μm. (**C**) Western blot analysis of HeLa cells coexpressing CERT-GFP WT or mutants with CSNK1G2-HA or PP2Cε-HA (n = 3). C, cluster (as represented in Figure 1).

12 reduced sphingolipid synthesis more than 80% (similar to what was obtained by treating cells with Myr) in HeLa cells but had no effect on *CERT1*-KO cells, in which sphingolipid synthesis was already greatly reduced (Supplemental Figure 5B).

We confirmed the metabolic alterations induced by overexpression of *CERT1* mutants in *CERT1*-KO cells in patient-derived fibroblasts bearing the p.G243R mutation and lymphoblasts bearing the p.T166A mutation. Patient cells produced substantially higher amounts of dhSM and dhCer than did their WT counterparts (Supplemental Figure 5, C and E). In contrast, inhibition of CERT activity with HPA-12 markedly reduced total dhCer and dhSM in both WT and patient-derived cells.

We observed a similar profile in steady-state sphingolipid levels and new synthesis when we examined patient cells after labeling with D_3-^{15}N-serine (Supplemental Figure 5, D and F). SA+3 backbone levels were much higher in patient-derived cells than in controls. The increase in sphingolipid synthesis observed in patients' cells was blocked by the administration of HPA-12, confirming that these effects are indeed caused by altered CERT activity (Supplemental Figures 4 and 5).

These data indicate that CERT activity is inherently coupled to the homeostatic regulation of de novo sphingolipid synthesis and suggest that frequent CerTra mutations cause an increase in CERT activity (Figure 4D).

CerTra mutations reveal an uncharacterized structural domain in CERT

The structures of the PH and START domains of CERT have been solved independently and as a complex (20, 38, 39), but little is known about the region between these 2 domains. It has been assumed to be largely unstructured except for a predicted coiled-coil segment that mediates CERT oligomerization upon UV irradiation (40, 41). Given the appreciable effect of CERT mutations in clusters 2 and 3 (Figure 1C), we decided to explore the structural context of these clusters. To this end, we subjected recombinant CERT to hydrogen-deuterium (H/D) exchange mass spectrometry (HDX-MS), which allows the study of protein dynamics and folding by assessing the solvent accessibility of protein surfaces (42, 43).

As expected, the HDX-MS profile of CERT highlighted the presence of amides protected from H/D exchange at early time points of exchange at the N- and C-terminal regions, corresponding to the PH (aa 23–117) and START (aa 389–618) globular domains (Figure 5, A and B). The areas from aa 187 to 218 and from aa 300 to 381 were highly accessible to solvent and

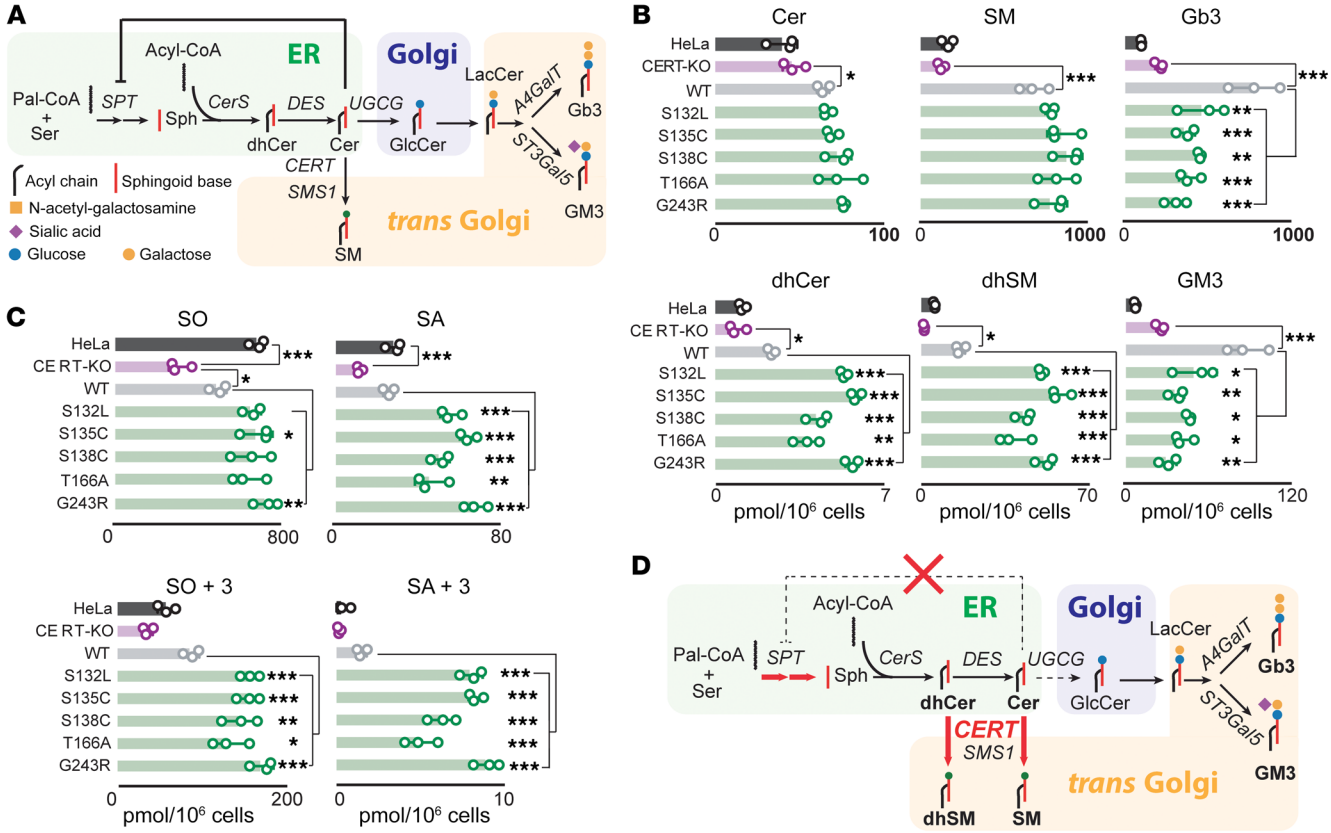

Figure 4. Several *CERT1* mutations increase sphingolipid levels. (**A**) Schematic representation of the de novo sphingolipid biosynthetic pathway with the main enzymes involved (shading indicates the prevalent intracellular localization of synthetic reactions). (**B**) Mass spectrometry profile of sphingolipids in HeLa *CERT1*-KO cells overexpressing selected *CERT1* mutants from clusters 1, 2, and 3. Values are total levels across the major fatty acid chain lengths of the indicated sphingolipids. The levels of individual species are reported in Supplemental Figure 4A. $n = 3$. Data are the mean ± SD. $^{*}P < 0.05$, $^{**}P < 0.01$, and $^{***}P < 0.001$, by 1-way ANOVA. (**C**) Effect on the LCB of CERT mutations in HeLa cells. LCB profiles were evaluated by incorporation of an isotope labeled (2,3,3-^{2}D,^{15}N)-L-serine. $n = 3$. Data are the mean ± SD. $^{*}P < 0.05$, $^{**}P < 0.01$, and $^{***}P < 0.001$, by 1-way ANOVA. (**D**) The de novo sphingolipid biosynthetic pathway as modified by *CERT1* mutations in clusters 1, 2, and 3. CerS, ceramide synthases; DES, dihydroceramide desaturase; SMS1, sphingomyelin synthase 1; UGCG, glucosylceramide synthase; ST3Gal5, GM3 synthase; A4GalT, Gb3 synthase; Sph, sphingolipid.

therefore probably contained no or a very dynamic secondary structure. Strikingly, regions encompassing cluster 2 and 3 mutations (i.e., aa 152–187 and aa 240–300) were heavily protected from exchange, indicating secondary structure formation and/or their engagement in protein-protein interactions (i.e., CERT oligomerization).

Structural modeling based on trRosetta (44) and AlphaFold (45) predicted the existence of 2 helices encompassing residues 154–187 (H1) and 242–304 (H2) (Figure 5C). Coiled-coil predictors (46) also suggested the existence of a coiled-coil region spanning part of H2 (aa 263–303) (Supplemental Figure 6A). Circular dichroism confirmed that purified CERT 151–309, hereafter called the CERT central core domain (CCD), and the synthetic peptides of H1 and H2 were indeed helical; the CCD had 60% helical content and a melting temperature of 43°C (Figure 5D).

Residue coevolution calculations using direct coupling analysis (44) on an ad hoc alignment supported a coiled-coil arrangement of H1 and H2, but the calculations also proposed pairs of contacting residues that could not be satisfied in the monomeric model (Supplemental Figure 6B). Interestingly, native MS (47) of the CERT CCD indicated that dimers predominate (theoretical MW of 18.5 kDa, observed MW of 37 kDa) (Figure 5E). When we evaluated the stoichiometry of recombinant full-length CERT with size-exclusion chromatography coupled to multiangle light scattering (SEC-MALS) (48), we found the absolute molar mass of the full-length CERT molecule to be, on average, 142.7 kDa, which, again, is compatible with a dimeric form (Supplemental Figure 6, C–F).

We therefore asked whether CERT dimerizes through its CCD domain. SEC-MALS analysis of the START domain alone (aa 389–618) indicated that it is a monomer, an oligomeric state also shared by the PH domain alone (26). By contrast, the construct encompassing the PH plus CCD domains (aa 1–341) was dimeric. Thus, although a recent study reported that CERT is organized as a homotrimer or a higher oligomer (49), our data strongly suggest that CERT dimerizes through its CCD (Supplemental Figure 6, D–F).

We then modeled the CCD dimer by rigid docking (see Supplemental Methods). Of the 6 best dimer models obtained, 5 had an antiparallel orientation (Supplemental Figure 6G, Supplemental Data Sets 1–7). Antiparallel orientation was also supported by coevolution restraints unexplained by the 3D model of the monomer (Figure 5F). However, not all predicted contacts are explained by a unique conformation, perhaps because the dimer is highly

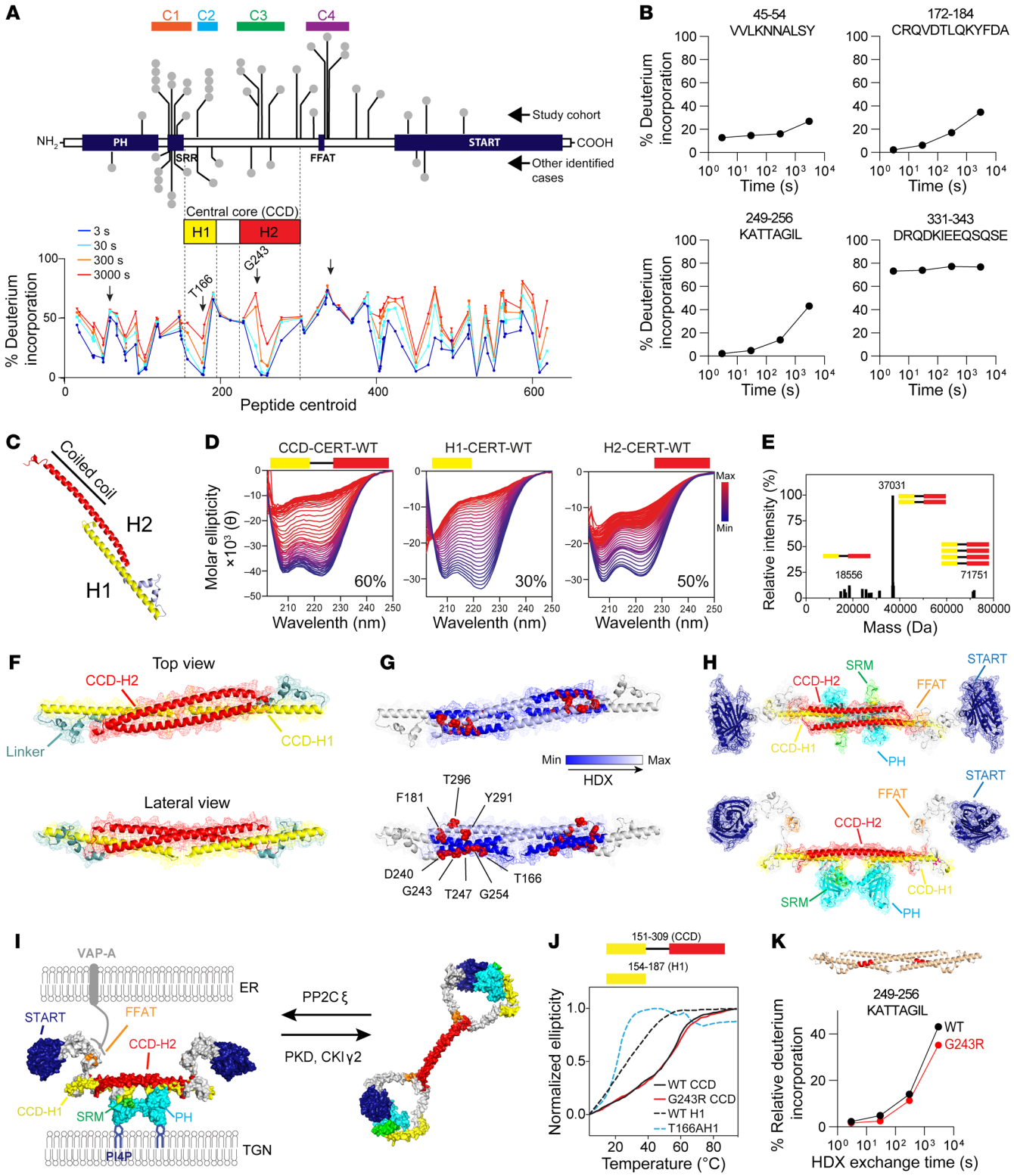
A
C1
C2
C3
C4
NH2
PH
SRR
FFAT
START
COOH
Study cohort
Other identified cases
Central core (CCD)
H1
H2
3 s
30 s
300 s
3000 s
T166
G243
% Deuterium incorporation
Peptide centroid
B
45-54
VVLKNNALSY
172-184
CRQVDTLQKYFDA
249-256
KATTAGIL
331-343
DRQDKIEEQSQSE
% Deuterium incorporation
Time (s)
C
Coiled coil
H2
H1
D
CCD-CERT-WT
H1-CERT-WT
H2-CERT-WT
Molar ellipticity ×10³ (Θ)
60%
30%
50%
Max
Min
Wavelength (nm)
E
Relative intensity (%)
37031
18556
71751
Mass (Da)
F
Top view
CCD-H2
CCD-H1
Linker
Lateral view
G
Min
Max
HDX
T296
F181
Y291
D240
G243
T247
G254
T166
H
START
SRM
CCD-H2
FFAT
CCD-H1
PH
I
VAP-A
ER
START
FFAT
CCD-H2
CCD-H1
SRM
PH
PI4P
TGN
PP2Cξ
PKD, CKIγ2
J
151-309 (CCD)
154-187 (H1)
Normalized ellipticity
WT CCD
G243R CCD
WT H1
T166AH1
Temperature (°C)
K
249-256
KATTAGIL
WT
G243R
% Relative deuterium incorporation
HDX exchange time (s)

Figure 5. Disease-causing *CERT1* mutations affect the central core structure of CERT. (**A**) Domain organization of CERT with its CCD and the predicted H1 and H2 helices. The global percentage of HDX is shown for all peptides graphed according to their central residue number. The mean of 3 experiments is shown. (**B**) Deuterium incorporation over time of 4 selected peptides (highlighted with arrows on the HDX profile). Data are from Supplemental Tables 5 and 6. (**C**) Molecular model of CERT's CCD based on contact prediction. Helix H1 is shown in yellow and H2 in red. (**D**) Thermostability of intervening regions showing a difference in HDX by circular dichroism: the samples were heated from 4°C to 94°C; the percentage indicates the helicity of each construct at 20°C. (**E**) Deconvoluted mass spectrum of purified recombinant CERT 151-309 WT. The value 18.5 kDa represents the molecular weight of the monomer, 37 kDa a dimer, and 71.5 kDa a tetramer. (**F**) Molecular model of CERT 151-309 WT as an antiparallel dimer. (**G**) Model showing the location of aa mutated in CerTra syndrome. The areas differentially exposed to deuterium exchange are indicated according to the color scale. (**H**) Molecular model of CERT WT as an antiparallel dimer. (**I**) Molecular model of CERT WT at the ER-TGN membrane contact site in its active and inactive conformations. (**J**) Thermostability of CERT 154-187 WT and p.T166A and CERT 151-309 WT and p.G243R by circular dichroism. (**K**) Peptide in the CCD displaying decreases in exchange in the p.G243R mutant compared with WT. These changes are mapped on the hypothetical CCD structure.

dynamic. Nonetheless, when CERT mutations were mapped onto the highest-scoring dimer model, they populated the interface between the H1 and H2 helices of the dimeric CCD, a region particularly protected from solvent as assessed by HDX-MS (Figure 5G). Here, residues p.D240, p.G243, p.T247, p.T251, and p.G254 define the side of the H2 helix that interfaces with H1 in the segment between p.T166 and p.F182, whereas p.Y291 and p.T296 form the H2 helix in the other CCD monomer contacting the same H1 portion with a different orientation (Figure 5G).On the basis of this new evidence, in addition to the existing x-ray structures and the CCD model, we propose the following 3D organization of the full-length CERT dimer: the dimer adopts a T-shaped conformation whereby the 2 PH domains are kept in close proximity at the extremity of the T stem, and the 2 START domains are at the extremities of the 2 T arms (Figure 5H and Supplemental File 6). Upon SRR phosphorylation, CERT undergoes a conformational change, such that the PH domain first interacts with the phosphorylated SRR (26) and then forms a complex with the START domain (20). In the context of our structural model, this conformational change implies a rearrangement of the interface between H1 and H2 of the CCD, which may be impaired by CerTra mutations that map to this region (Figure 5I).

We analyzed the effect of CERT mutations on the CCD structure and evaluated the melting curves of the synthetic peptides CERT 154–187 and purified CERT 151–309 WT and their mutant counterparts. We found that p.T166A decreased CERT H1 helicity and destabilized it, while p.G243R had negligible effects on CCD secondary structure and stability (Figure 5J and Supplemental Figure 6H). Nonetheless, when we compared the HDX profile of recombinant full-length CERT WT with p.G243R, we observed diminished solvent accessibility for the p.G243R mutant in a region encompassing aa 249–256 (Figure 5K), an H2 region coordinating with H1. This suggests that, rather than impairing CCD structure, p.G243R impairs CCD dynamics and possibly its interactions with other proteins. These results suggest a model whereby the CCD enables the conformational change that takes place upon CERT phosphorylation to deactivate the protein and signal that sufficient levels of SM production have been reached. CerTra-causing *CERT1* mutations in the CCD disturb this conformational change either by altering CCD stability (p.T166A) or CCD dynamics/interactions (p.G243R).

CERT gain of function alters sphingolipid metabolism, brain size, and locomotion in Drosophila melanogaster

Altogether, our data indicate that CerTra mutations disrupt CERT autoregulation, resulting in an inappropriate gain of CERT function and excessive sphingolipid production. To test whether this is sufficient to induce neurological manifestations in an animal model, we increased the *CERT1* dosage in *D. melanogaster*. The metabolic activity of *D. melanogaster* CERT (dCERT) is similar to that of mammalian CERT (50) and shares 43% sequence identity with human CERT, including all 6 of the most recurrent CerTra variants. We generated *D. melanogaster* strains on the w^{1118} background (hereafter referred to as control [Ctrl]) bearing 2 extra copies of either $dCERT^{WT}$ (hereafter referred to as +WT) or $dCERT^{p.S149L}$ (hereafter referred to as +SL; equivalent to the most common and severe CerTra mutation, p.S132L) under the control of its endogenous promoter (Figure 6A; see also Supplemental Methods).

Total *dCERT* mRNA levels were 50% higher than those in Ctrl flies in both +WT and +SL strains, with the increase being completely ascribable to the extra exogenous copies of *dCERT* (Figure 6B). The increased gene dosage did not shorten the lifespan of transgenic *Drosophila*; in fact, both the male and female animals lived slightly longer (Supplemental Figure 7A). The transgenic strains had wing and abdomen sizes comparable to those of Ctrl flies (Supplemental Figure 7B), but smaller heads and brains (Figure 6, C–G, and Supplemental Figure 7, C and D). Feeding HPA-12 to +WT and +SL larvae (see Supplemental Methods) restored head size, suggesting that increased *dCERT* activity was responsible for this phenotype (Figure 6F). The levels of Cer and dhCer were significantly and similarly increased in both +WT and +SL strains. Cer-phosphoethanolamine (CPE, the *Drosophila* equivalent of mammalian SM) (51) and dihydroceraminde (dhCPE) levels were also increased in both strains, but more substantially in the +SL strain (Figure 6H and Supplemental Figure 7, E–G). These changes were similar to those observed in whole *Drosophila* bodies (Supplemental Figure 7E) and resembled those we observed in mammalian cells (Figure 2B), suggesting that *dCERT* gain of function affects sphingolipid metabolism in flies in a manner similar to the effects of CerTra mutations in humans. It is worth noting that glycosphingolipid levels were not significantly altered in +WT or +SL strains, suggesting that changes in Cer, CPE, and their dihydro counterparts were sufficient to induce neurological phenotypes in these strains (Supplemental Figure 7E).

As most patients with CerTra experience motor delay, we monitored the locomotor activity of the +WT and +SL flies (52). Both +WT and +SL flies showed locomotor hypoactivity compared with Ctrl flies (Figure 6I). Pretreatment with HPA-12 (10 μM) for 7 days, which reduced sphingolipid levels (Supplemental Figure 7H), rescued this phenotype in the transgenic lines but had little effect on Ctrl flies (Figure 6J). Moreover, HPA-12 treatment had no effect on

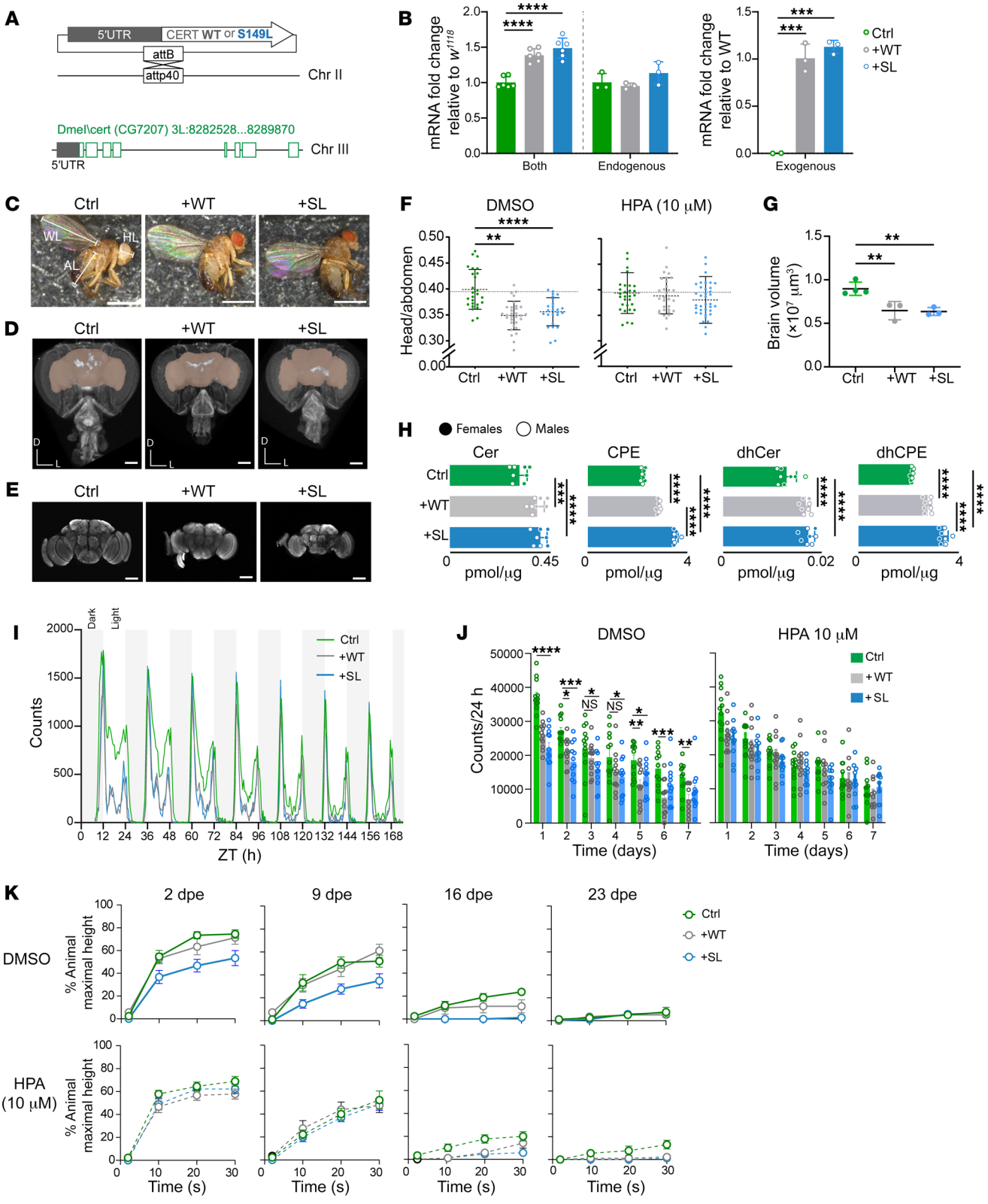
A
5′UTR
CERT WT or S149L
attB
attp40
Chr II
Dmel\cert (CG7207) 3L:8282528...8289870
Chr III
5′UTR
B
mRNA fold change relative to w1118
Both
Endogenous
mRNA fold change relative to WT
Exogenous
Ctrl
+WT
+SL
C
Ctrl
+WT
+SL
WL
HL
AL
D
Ctrl
+WT
+SL
E
Ctrl
+WT
+SL
F
DMSO
HPA (10 μM)
Head/abdomen
G
Brain volume (×10^7 μm^3)
H
Females
Males
Cer
CPE
dhCer
dhCPE
pmol/μg
I
Dark
Light
Counts
ZT (h)
J
DMSO
HPA 10 μM
Counts/24 h
Time (days)
K
2 dpe
9 dpe
16 dpe
23 dpe
DMSO
HPA (10 μM)
% Animal maximal height
Time (s)

Figure 6. CERT gain of function causes neurological defects in *D. melanogaster*. (**A**) Schematic of transgenic *dCERT* flies on the w^{1118} background. $dCERT^{WT}$, +WT; $dCERT^{p.S149L}$, +SL; Chr, chromosome. (**B**) Quantification of endogenous or exogenous *dCERT* mRNA levels in flies on the w^{1118} background (Ctrl) in *dCERT*-transgenic flies. Data indicate the $\log_2$ fold change over Ctrl or +WT (n = 6; data are the mean ± SD). (**C**) Representative specimens of Ctrl, +WT, and +SL adult flies. Head length (HL), abdomen length (AL), and wing length (WL) were measured. Scale bars: 1 mm. (**D**) 3D rendering of a micro-CT scan of the heads from Ctrl, +WT, and +SL adults (frontal view). Brain volume is highlighted in pink. Body axes are dorsal (**D**) and left (L). Scale bars: 100 μm. (**E**) *Z*-projections of confocal stacks of whole-mount adult Ctrl, +WT, and +SL adult brains (frontal view) immunostained with anti-nc82. Scale bars: 100 μm. (**F**) HL/AL ratio of flies reared on DMSO or 10 μM HPA-12 (HPA) (Ctrl, n = 26 or 30, +WT n = 31 or 31, and +SL, n = 25 or 38). (**G**) Brain volume for Ctrl, +WT, and +SL flies as determined by confocal microscopy (n = 3–4; data are the mean ± SEM). (**H**) Mass spectrometry profile of sphingolipids in Ctrl, +WT, and +SL adult heads (n = 8). (**I**) Locomotion of Ctrl, +WT, and +SL flies plotted as total counts per 30 minutes over time (n = 16). (**J**) Locomotion of flies pretreated with 0 or 10 μM HPA-12 (n = 12). (**K**) Climbing ability of flies at 2, 9, 16, and 23 days post eclosion (dpe) after vigorous mechanical stress (n = 9). Data shown are the mean ± SEM. $^*P < 0.05$, $^{**}P < 0.01$, $^{***}P < 0.001$, and $^{****}P < 0.0001$, by 1-way ANOVA.

the locomotion of a w^{1118} derivative *Drosophila* strain bearing a large chromosomal defect in which the *dCERT* gene was deleted (hereafter referred to as KO) (Supplemental Figure 7I), suggesting that the HPA-12 effect on locomotion requires *dCERT* expression.

Although the +WT and +SL strains share motor hypoactivity, they do have distinct metabolic phenotypes (Figure 6H), which we hypothesized should produce some difference in phenotype. Because patients with CerTra frequently have seizures, we decided to look for seizure-like reactions, such as the paralysis that seizure-susceptible flies often experience after vigorous mechanical stimulation (53, 54). Our strains did not exhibit paralysis upon mechanical stimulation, but the +SL flies showed impaired negative geotaxis that could be corrected by HPA-12 treatment (Figure 6K). Notably, negative geotaxis in nonstressed animals was indistinguishable across genotypes (Supplemental Figure 7J).

These data indicate that an increase in *dCERT* activity in *Drosophila* induced sphingolipid metabolic changes similar to those observed in CerTra syndrome, impaired locomotion, and caused central nervous system vulnerability to mechanical shock in the most severely affected line.

Discussion

In this study, we report that multiple de novo heterozygous variants in *CERT1* caused an autosomal dominant developmental syndrome we named CerTra, which is characterized by various degrees of developmental delay, motor delay, cognitive impairment, behavioral abnormalities, and seizures. Several CerTra mutations reduce or abolish the capability of CERT to be inactivated in response to excessive SM production. This leads to uncontrolled Cer transfer out of the ER, with several consequences: (a) reduced Cer at the ER relaxes the homeostatic inhibition of SPT (55, 56), resulting in increased de novo sphingolipid synthesis; (b) reduced Cer at the Golgi, the site for glucosylceramide synthesis, impairs glycosphingolipid production; and (c) excessive CERT activity likely competes with Cer desaturase activity at the ER, leading to the transfer of a significant amount of dhCer to the *trans* Golgi and production of dhSM. Elevated dihydrosphingolipid levels cause neuropathology. For example, biallelic loss-of-function mutations in *DEGS1*, which catalyzes the final conversion of dhCer to Cer (Figure 2A), result in increased dihydrosphingolipid levels, causing a multisystem neurological disorder of both the central and peripheral nervous systems, characterized by hypomyelination and leukodystrophy (MIM #618404) (57, 58). Recessively inherited loss-of-function mutations in alkaline ceramidase 3 (*ACER3*) also result in increased dihydrosphingolipid formation and a leukodystrophy phenotype (MIM #617762) (59). Impaired glycosphingolipid synthesis is a further cause of neuropathology: loss-of-function mutations in *ST3GAL5* or *B4GALNT1*, which encode 2 key enzymes in ganglio-series glycosphingolipid synthesis (i.e., GM3 and GM2 synthases), cause neurodevelopmental regression (MIM #609056) and spastic paraplegia (MIM #609195), respectively (60–65). Recently, a specific group of mutations in SPT subunits were reported to cause childhood-onset amyotrophic lateral sclerosis (66–68) and hereditary spastic paraplegia (69). All identified mutations disturbed the homeostatic control of de novo sphingolipid synthesis, resulting in greatly elevated sphingolipid levels.

Several CerTra mutations cause lipid metabolic derangements similar to those associated with the above-listed conditions, nonetheless, the molecular mechanisms of CERT dysregulation appear to be varied. Mutations in the SRR directly impair CERT-inactivating phosphorylation, whereas mutations in the CCD hinder the conformational change that follows this event. We have not directly addressed the effects of other mutations close to the FFAT motif or in the PH and START domains. These mutations likely affect CERT interaction with VAP proteins (70) and the final events of CERT inactivation that involve intramolecular interactions between the PH and START domains (24). Four consecutive variants (p.R366T, p.I381V, p.E424G, and p.A449V) do not affect CERT localization or the phosphorylation state. When analyzed in greater depth, these variants present some doubts about their actual pathogenicity: (a) each of them is associated with a single patient, and they are not part of a recognizable cluster of mutations; (b) p.I381V has been found in 1 healthy individual; (c) p.A449V has been found in an individual whose mother and father presented with intellectual disability independently of the mutational state of *CERT1*; (d) p.R366T has been found in an individual for whom the very little information we have would point toward a very mild phenotype. Further studies will be required to assess the actual role of these variants and, more in general, to untangle the cellular mechanisms by which sphingolipid metabolism disruption leads to CerTra syndrome. Nonetheless, the characterization of this rare disease entity and of the most frequent variants associated with it has already revealed unforeseen operating principles of sphingolipid homeostasis, led to the definition of a new structural region in CERT, and delineated a possible use of CERT inhibitors for the treatment of patients with CerTra.

Methods

Study participant identification and clinical characterization

Initial screening and identification of anonymized individuals harboring *CERT1* variation was conducted using the following public data-

bases and tools: ClinVar (https://www.ncbi.nlm.nih.gov/clinvar/), Decipher (71), GeneMatcher (72), and VKGL-NL Rotterdam (https://www.vkgl.nl/nl/) (Supplemental Table 1). Each patient underwent a full clinical examination by a neurologist and/or medical geneticist. Clinical data were directly abstracted from medical records provided by the referring clinicians and included a behavioral assessment and EEGs. Developmental delay and cognitive ability tests were performed on patients using the following tests: Gesell Developmental Schedules, the Chinese National Health Commission Developmental Evaluation Scale, the Wechsler Intelligence Scale for Children, the Peabody Picture Vocabulary Test, 4th Edition (PPVT-4), and Bayley Scales of Infant Development II. When possible, a standardized assessment of impairment in conceptual, social, and practical domains for each patient was performed in accordance with the DSM-5 and noted to be mild, moderate, severe, or profound. The degrees of intellectual disability were classified according to the following verbal and nonverbal IQ scores: mild (IQ of 50–55 to ~70), moderate (IQ of 35–40 to 50–55), severe (IQ of 20–25 to 35–40), and profound (IQ below 20–25).

To characterize craniofacial/skeletal dysmorphia, we performed a deep phenotyping analysis for all of the patients whose families agreed to provide photographs. This was done by the team of Eva Bermejo-Sánchez at the Institute of Rare Disease Research (IIER) in Madrid, Spain. Dysmorphology analyses were performed by experimenters blinded to the variant detected for each patient. Each parameter was compared with age-, sex-, and ethnicity-matched healthy individuals. Briefly, a detailed reading of all the clinical reports was performed to extract a first list of dysmorphic features that was then used to evaluate all of the patients. All the available photographs were assessed on the basis of those features, giving a matrix of 96 rows that were scrutinized for all patients. Thus, the same traits were assessed by the same observer using homogeneous criteria for all the patients. See the Supplemental Clinical Appendix for all the features for each patient.

Pathogenicity analysis

All identified variants were analyzed in accordance with American College of Medical Genetics and Genomics (ACMG) guidelines for variant interpretation and classification (73). Minor allele frequencies (MAFs) of all *CERT1* variants were obtained from gnomAD (74), BRowse All Variants Online (BRAVO) (https://bravo.sph.umich.edu), and 1000 Genomes Project (https://www.genome.gov/27528684/1000-genomes-project). Functional annotation of variants was carried out with ANNOtate VARiation (ANNOVAR) (75) using M-CAP (76), REVEL (77), Eigen (78), and CADD (78) pathogenicity scores. As a general guideline, pathogenicity is predicted for variants with scores over 0.025 for M-CAP, over 0.5 for REVEL, over 0.5 for Eigen, and over 20 for CADD. Prediction scores for CerTra variants were compared with other missense variants found in singleton cases among the general population in gnomAD (i.e., missense variants reported in only 1 healthy individual in gnomAD).

The analysis of variant clustering was performed as previously described (17, 79). In short, to determine whether the observed variants in patients (17 positions) cluster linearly more than expected compared with random permutations, we calculated the geometric mean distance (δg) between all missense variants on the *CERT1* gene. We calculated δg by taking the mean distance normalized for the transcript length of *CERT1* (hg19:NM_005713.3) over all variant combinations of x_i and x_j of the missense variants, where x represents the position for variants i and j, respectively. A total of 1×10^8 permutations were performed, and statistical significance was determined (Fisher's exact test) on the basis of how many times the permuted mean distance was smaller or equal to the mean geometric distance observed in our cohort (i.e., significant clustering was determined if the permuted mean distance was larger than what was observed in our cohort).

Immunofluorescence staining and image analysis

HeLa cells were grown on glass coverslips that were treated according to the experimental protocol, fixed with 4% paraformaldehyde for 15 minutes at room temperature (RT), and washed 3 times with PBS. After fixation, cells were blocked with 5% BSA and permeabilized with 0.5% saponin for 20 minutes at RT, followed by a 1-hour incubation with selected antibodies against the antigen of interest in the blocking solution. Cells were then washed 3 times with PBS and incubated with the appropriate isotype-matched, Alexa Fluor–conjugated secondary antibodies diluted in blocking solution for 30 minutes. After immunostaining, cells were washed 3 times in PBS and once in water to remove salts. After Hoechst staining for nuclei, the samples were mounted with Fluoromount-G (Southern Biotech, 0100-01) on glass microscope slides and analyzed under a Leica SP8 confocal microscope with a 63× oil objective (1.4 NA),a Zeiss LSM700 with a 40× oil objective (1.3 NA), or a Stellaris-5 with a 40× oil objective (1.3 NA). Optical confocal sections were taken at 1 Airy unit under nonsaturated conditions with a resolution of 1,024 × 1,024 pixels and a frame average of 2. Images were then processed using Fiji software (https://imagej.net/Fiji) (80).

Statistics

Experimental design. For quantification of protein expression in patient-derived cell lines, values from at least 3 independent experiments were used. At every stage of the study, the experimenter was blinded to the identity of the control and patient-derived cell lines. For example, experimenter 1 made a list of samples and controls to be tested, and experimenter 2 randomized this list and relabeled the tubes; experimenter 2 was the only person with the key to identification of the samples. These samples were then distributed to experimenter 3 to culture the cells, and then to experimenter 1 to perform Western blot analysis, and finally, experimenters 1 and 4 analyzed the data. Only then was the key applied to identify the samples.

Software and statistical analysis. Statistical significance ($P < 0.05$) was analyzed using GraphPad Prism 8 (GraphPad Software), Excel (Microsoft), and R-4.2.3 (The R Project for Statistical Computing). Statistical details and the number of replicates for each experiment can be found in the figures and legends. The range of expression levels in Western blots was determined from at least 3 independent experiments. The Student's t test was used to compare the means between 2 groups, and ANOVA was used to compare the means among more than 2 groups.

Study approval

All study procedures were defined under protocol no. AAAS7401, which was approved by the IRB of Columbia University Irving Medical Center (VAG); the Cambridgeshire Research Ethics Committee for the whole of the United Kingdom; the IRB "Commissie MensgebondenOnderzoek Regio Arnhem-Nijmegen" under protocol no. 2011/188; the Hospital Universitario "Virgen de la Arrixaca," Wro-

claw Medical University; San Gerardo Hospital (Monza, Italy); Children's Health Ireland at Temple Street Hospital (Dublin, Ireland); the ethics committee of the Medical Faculty at Leipzig University (224/16-ek and 402/16-ek); and the ethics committee of the Instituto de Salud Carlos III.

Full study enrollment (i.e., acquisition of clinical data for further analysis) was conducted only after written, informed consent/assent was obtained for each study participant. The study also adhered to tenets outlined by the Declaration of Helsinki. All patient-related study procedures were conducted according to the respective ethics committees of each participating institution. Specific written, informed consent was also acquired for all participants whose photographs appear in the manuscript.

Data availability

This study made use of data generated by the DEFIDIAG study sponsored by the INSERM (France). A full list of centers that contributed to the generation of the data is available from https://defidiag.inserm.fr/ and via email from c16-110.coordo.isp@inserm.fr. This work also used Simons Simplex Collection (SSC) data including whole-exome sequencing (raw and processed) and associated phenotypic data obtained through Simons Foundation Autism Research Initiative (SFARI) Base (SFARI Request ID: 12030.1.1). This study makes use of data generated by the DECIPHER community. A full list of centers that contributed to the generation of the data is available at https://deciphergenomics.org/about/stats and via email from contact@deciphergenomics.org.

Author contributions

C Gehin, MAL, and LC designed and performed experiments, analyzed and interpreted the data, and drafted the manuscript. WL collected all clinical symptoms, analyzed and interpreted clinical data, and drafted the manuscript. SH supported experimental work and contributed to the writing of the manuscript. SZ and LAA performed structural simulations. VK provided recombinant PKD. BEM performed the HDX-MS. JEB performed and supervised HDX-MS. AV provided technical support. PH synthesized synthetic peptides. KH and TY provided *CERT1*-KO cell lines. PDLR supervised the structural simulations. BL, SR, JPB, and ER designed the *Drosophila* lines. BDM designed and supervised the behavioral tests with *Drosophila*. MVC designed and constructed the apparatus used for the negative geotaxis assay. SB supervised and supported the micro-CT experiment under the supervision of AMJ. YG, TYL, and SSC performed the ASD association analysis. EHG provided patient-derived fibroblasts and unaffected, healthy age- and sex-matched fibroblasts for participant 14. ELM and EBS performed craniofacial/skeletal deep phenotyping analysis. EHG, APAS, JHS, HG, KX, QZ, SX, CRF, CPB, MJL, MB, NSC, VW, ELM, EBS, BMD, RO, BP, VS, DG, MM, AS, AT, YH, MHW, FS, A Murgia, EL, RS, CG, RP, CZ, CK, VLG, LAD, IK, ERJ, IV, PFA, AG, ALB, FTMT, GC, PK, AMA, A Marwaha, NLC, MJF, EBR, VKG, VMS, BWVB, and MAB provided clinical data, genetic information, variant revalidation, and comments on the manuscript. ABRM and JMB interpreted and analyzed the MRI data. TH, GD, and VAG conceived the study, analyzed and interpreted the data, and wrote the manuscript. All authors approved the final version of the manuscript.

Acknowledgments

We sincerely thank the families who participated in this study and all the staff involved in patient care. We thank Dimitri Moreau and Stefania Vossio (ACCESS Geneva) for microscopy and data analysis; Natalia Gasilova (EPFL ISIC Valais) for native MS; the Correia laboratory at EPFL for support with SEC-MALS; and the BIOP, PPSCF, and PCF Research Core Facilities at the School of Life Sciences of EPFL, Fani Deverni (FLEXLAB, STI, EPFL) for micro-CT. We also thank M. Chorpra, I.A. Carrera, I. Cusco, and B. Molloy (Genuity Science, Ireland Ltd., Dublin/CHI at Temple Street Rare Disease Research Programme), as well as K. Gorman (CHI at Temple Street, Dublin, Ireland), M. Posada, J. Alonso, I.A. Carrera, and the entire SpainUDP consortium for help with molecular genetic testing and helpful clinical consultation. We also thank the Undiagnosed Diseases Network International (UDNI) for data sharing. We thank members of the Hornemann, D'Angelo, and Gennarino laboratories for helpful discussions, G. Karsenty for critical comments on the manuscript, and V. Brandt for rigorous editing.

This work was supported by the National Institute of Neurological Disorders and Stroke (NINDS), NIH (R01NS109858, to VAG); the Paul A. Marks Scholar Program at the Columbia University Vagelos College of Physicians and Surgeons (to VAG); a TIGER grant from the TAUB Institute at the Columbia Vagelos College of Physicians and Scientists (to VAG); the Swiss National Science Foundation (SNF 31003A-179371, to TH); the European Joint Program on Rare Diseases (EJP RD+SNF 32ER30-187505, to TH); the Swiss Cancer League (KFS-4999-02-2020, to GD); the EPFL institutional fund (to GD); the Kristian Gerhard Jebsen Foundation (to GD); the Swiss National Science Foundation (SNSF) (310030_184926, to GD); the Swiss Foundation for Research on Muscle Disease (FSRMM, to MAL); the Natural Science and Engineering Research Council of Canada (Discovery Grant 2020-04241, to JEB); the Italian Ministry of Health Young Investigator Grant (GR-2011-02347754, to EL); the Fondazione Istituto di Ricerca Pediatrica – Città della Speranza (18-04, to EL); the Wroclaw Medical University (SUB.E160.21.004, to RS); the National Science Centre, Poland (2017/27/B/NZ5/0222, to RS); Telethon Undiagnosed Diseases Program (TUDP) (GSP15001); the Temple Street Foundation/Children's Health Foundation Ireland (RPAC 19-02, to IK); the Deutsche Forschungsgemeinschaft (DFG) (PO2366/2–1, to BP); the Instituto de Salud Carlos III, Spain (to ELM, EBS, and BMD); the National Natural Science Foundation of China (81871079 and 81730036, to HG and KX); and the National Institutes of Diabetes and Digestive and Kidney Diseases (NIDDK), NIH (R01 DK115574, to SSC).

The DEFIDIAG study is funded by grants from the French Ministry of Health in the framewok of the national French initiative for genomic medicine. The funders were not involved in the study design, data acquisition, analysis, or writing of the manuscript. Funding for the DECIPHER project was provided by Wellcome. The DDD study presents independent research commissioned by the Health Innovation Challenge Fund (grant number HICF-1009-003), a parallel funding partnership between Wellcome and the Department of Health, and the Wellcome Sanger Institute (grant number WT098051). The views expressed in this publication are those of the author(s) and not necessarily those of Wellcome or the Department of Health. The study has UK Research Ethics Committee approval (10/H0305/83, granted

by the Cambridge South REC, and GEN/284/12, granted by the Republic of Ireland REC). The research team acknowledges the support of the National Institute for Health Research, through the Comprehensive Clinical Research Network.

Address correspondence to: Thorsten Hornemann, Clinical Chemistry (IKC), USZ WAGI, Wagistrasse 14, CH-8952 Schlieren, Switzerland. Phone: 41.44.556.3101; Email: thorsten.hornemann@usz.ch. Or to: Giovanni D'Angelo, EPFL, SV/IBI/UPDANGELO, Station 19, CH-1015 Lausanne, Switzerland. Phone: 41.21.693.4276; Email: giovanni.dangelo@epfl.ch. Or to: Vincenzo A. Gennarino, Department of Genetics and Development (CUIMC), 701 West 168th Street, HHSC 1402, New York, New York 10032, USA. Phone: 1.212.305.7863; Email: vag2138@cumc.columbia.edu.

1. Dunn TM, et al. A perilous path: the inborn errors of sphingolipid metabolism. *J Lipid Res*. 2019;60(3):475–483.
2. Hannun YA, Obeid LM. Sphingolipids and their metabolism in physiology and disease. *Nat Rev Mol Cell Biol*. 2018;19(3):175–191.
3. Ozkara HA. Recent advances in the biochemistry and genetics of sphingolipidoses. *Brain Dev*. 2004;26(8):497–505.
4. Sabourdy F, et al. Monogenic neurological disorders of sphingolipid metabolism. *Biochim Biophys Acta*. 2015;1851(8):1040–1051.
5. Breslow DK, Weissman JS. Membranes in balance: mechanisms of sphingolipid homeostasis. *Mol Cell*. 2010;40(2):267–279.
6. Hanada K, et al. Molecular machinery for non-vesicular trafficking of ceramide. *Nature*. 2003;426(6968):803–809.
7. Fugmann T, et al. Regulation of secretory transport by protein kinase D-mediated phosphorylation of the ceramide transfer protein. *J Cell Biol*. 2007;178(1):15–22.
8. de Ligt J, et al. Diagnostic exome sequencing in persons with severe intellectual disability. *N Engl J Med*. 2012;367(20):1921–1929.
9. De Rubeis S, et al. Synaptic, transcriptional and chromatin genes disrupted in autism. *Nature*. 2014;515(7526):209–215.
10. Hamdan FF, et al. De novo mutations in moderate or severe intellectual disability. *PLoS Genet*. 2014;10(10):e1004772.
11. Helbig KL, et al. Diagnostic exome sequencing provides a molecular diagnosis for a significant proportion of patients with epilepsy. *Genet Med*. 2016;18(9):898–905.
12. Iossifov I, et al. The contribution of de novo coding mutations to autism spectrum disorder. *Nature*. 2014;515(7526):216–221.
13. Murakami H, et al. Intellectual disability-associated gain-of-function mutations in CERT1 that encodes the ceramide transport protein CERT. *PLoS One*. 2020;15(12):e0243980.
14. The Deciphering Developmental Disorders Study. Large-scale discovery of novel genetic causes of developmental disorders. *Nature*. 2015;519(7542):223–228.
15. Takata A, et al. Integrative analyses of de novo mutations provide deeper biological insights into autism spectrum disorder. *Cell Rep*. 2018;22(3):734–747.
16. Wang T, et al. De novo genic mutations among a Chinese autism spectrum disorder cohort. *Nat Commun*. 2016;7:13316.
17. Lee W, et al. Identifying patients and assessing variant pathogenicity for an autosomal dominant disease-driving gene. *STAR Protoc*. 2022;3(1):101150.
18. APA, eds. *Diagnostic and Statistical Manual of Mental Disorders*. 5th ed. American Psychiatric Association. 2013.
19. Satterstrom FK, et al. Large-scale exome sequencing study implicates both developmental and functional changes in the neurobiology of autism. *Cell*. 2020;180(3):568–584.
20. Prashek J, et al. Interaction between the PH and START domains of ceramide transfer protein competes with phosphatidylinositol 4-phosphate binding by the PH domain. *J Biol Chem*. 2017;292(34):14217–14228.
21. Baron CL, Malhotra V. Role of diacylglycerol in PKD recruitment to the TGN and protein transport to the plasma membrane. *Science*. 2002;295(5553):325–328.
22. Capasso S, et al. Sphingolipid metabolic flow controls phosphoinositide turnover at the *trans*-Golgi network. *EMBO J*. 2017;36(12):1736–1754.
23. Luberto C, Hannun YA. Sphingomyelin synthase, a potential regulator of intracellular levels of ceramide and diacylglycerol during SV40 transformation. Does sphingomyelin synthase account for the putative phosphatidylcholine-specific phospholipase C? *J Biol Chem*. 1998;273(23):14550–14559.
24. Kumagai K, et al. Interorganelle trafficking of ceramide is regulated by phosphorylation-dependent cooperativity between the PH and START domains of CERT. *J Biol Chem*. 2007;282(24):17758–17766.
25. Prashek J, et al. Crystal structure of the pleckstrin homology domain from the ceramide transfer protein: implications for conformational change upon ligand binding. *PLoS One*. 2013;8(11):e79590.
26. Sugiki T, et al. Phosphoinositide binding by the PH domain in ceramide transfer protein (CERT) is inhibited by hyperphosphorylation of an adjacent serine-repeat motif. *J Biol Chem*. 2018;293(28):11206–11217.
27. Tomishige N, et al. Casein kinase I{gamma}2 down-regulates trafficking of ceramide in the synthesis of sphingomyelin. *Mol Biol Cell*. 2009;20(1):348–357.
28. Thomaseth C, et al. Modeling sphingomyelin synthase 1 driven reaction at the Golgi apparatus can explain data by inclusion of a positive feedback mechanism. *J Theor Biol*. 2013;337:174–180.
29. Saito S, et al. Protein phosphatase 2Cε is an endoplasmic reticulum integral membrane protein that dephosphorylates the ceramide transport protein CERT to enhance its association with organelle membranes*. *J Biol Chem*. 2008;283(10):6584–6593.
30. Tamura N, et al. Intellectual-disability-associated mutations in the ceramide transport protein gene CERT1 lead to aberrant function and subcellular distribution. *J Biol Chem*. 2021;297(5):101338.
31. Goto A, et al. Involvement of a cluster of basic amino acids in phosphorylation-dependent functional repression of the ceramide transport protein CERT. *Int J Mol Sci*. 2022;23(15):8576.
32. Lone MA, et al. Subunit composition of the mammalian serine-palmitoyltransferase defines the spectrum of straight and methyl-branched long-chain bases. *Proc Natl Acad Sci U S A*. 2020;117(27):15591–15598.
33. Ternes P, et al. Identification and characterization of a sphingolipid delta 4-desaturase family. *J Biol Chem*. 2002;277(28):25512–25518.
34. Wang Y, et al. Structural insights into the regulation of human serine palmitoyltransferase complexes. *Nat Struct Mol Biol*. 2021;28(3):240–248.
35. Yamaji T, Hanada K. Establishment of HeLa cell mutants deficient in sphingolipid-related genes using TALENs. *PLoS One*. 2014;9(2):e88124.
36. Davis DL, et al. The ORMDL/Orm–serine palmitoyltransferase (SPT) complex is directly regulated by ceramide: reconstitution of SPT regulation in isolated membranes. *J Biol Chem*. 2019;294(13):5146–5156.
37. Yasuda S, et al. A novel inhibitor of ceramide trafficking from the endoplasmic reticulum to the site of sphingomyelin synthesis. *J Biol Chem*. 2001;276(47):43994–44002.
38. Kudo N, et al. Structural basis for specific lipid recognition by CERT responsible for nonvesicular trafficking of ceramide. *Proc Natl Acad Sci U S A*. 2008;105(2):488–493.
39. Sugiki T, et al. Structural basis for the Golgi association by the pleckstrin homology domain of the ceramide trafficking protein (CERT). *J Biol Chem*. 2012;287(40):33706–33718.
40. Charruyer A, et al. Decreased ceramide transport protein (CERT) function alters sphingomyelin production following UVB irradiation. *J Biol Chem*. 2008;283(24):16682–16692.
41. UniProt Consortium. UniProt: a worldwide hub of protein knowledge. *Nucleic Acids Res*. 2019;47:506–515.
42. Engen JR, et al. Developments in hydrogen/deuterium exchange mass spectrometry. *Anal Chem*. 2021;93(1):567–582.
43. Masson GR, et al. Recommendations for performing, interpreting and reporting hydrogen deuterium exchange mass spectrometry (HDX-MS) experiments. *Nat Methods*. 2019;16(7):595–602.
44. Yang J, et al. Improved protein structure prediction using predicted interresidue orientations. *Proc Natl Acad Sci U S A*. 2020;117(3):1496–1503.
45. Jumper J, et al. Highly accurate protein structure prediction with AlphaFold. *Nature*. 2021;596(7873):583–589.
46. Trigg J, et al. Multicoil2: predicting coiled coils and their oligomerization states from sequence in the twilight zone. *PLoS One*. 2011;6(8):e23519.

47. van den Heuvel RHH, Heck AJR. Native protein mass spectrometry: from intact oligomers to functional machineries. *Curr Opin Chem Biol*. 2004;8(5):519–526.
48. Mogridge J. Using light scattering to determine the stoichiometry of protein complexes. In: Meyerkord CL, Fu H, eds. *Protein-Protein Interactions: Methods and Applications*. Springer New York; 2015:233–238.
49. Revert F, et al. Selective targeting of collagen IV in the cancer cell microenvironment reduces tumor burden. *Oncotarget*. 2018;9(13):11020–11045.
50. Rao RP, et al. Ceramide transfer protein function is essential for normal oxidative stress response and lifespan. *Proc Natl Acad Sci U S A*. 2007;104(27):11364–11369.
51. Rietveld A, et al. Association of sterol- and glycosylphosphatidylinositol-linked proteins with Drosophila raft lipid microdomains. *J Biol Chem*. 1999;274(17):12049–12054.
52. Pfeiffenberger C, et al. Locomotor activity level monitoring using the *Drosophila* Activity Monitoring (DAM) system. *Cold Spring Harb Protoc*. 2010;2010(11):pdb prot5518.
53. Benzer S. From the gene to behavior. *JAMA*. 1971;218(7):1015–1022.
54. Pavlidis P, et al. The Drosophila easily shocked gene: a mutation in a phospholipid synthetic pathway causes seizure, neuronal failure, and paralysis. *Cell*. 1994;79(1):23–33.
55. Breslow DK, et al. Orm family proteins mediate sphingolipid homeostasis. *Nature*. 2010;463(7284):1048–1053.
56. Clarke BA, et al. The *Ormdl* genes regulate the sphingolipid synthesis pathway to ensure proper myelination and neurologic function in mice. *Elife*. 2019;8:e51067.
57. Karsai G, et al. DEGS1-associated aberrant sphingolipid metabolism impairs nervous system function in humans. *J Clin Invest*. 2019;129(3):1229–1239.
58. Pant DC, et al. Ceramide signalling in inherited and multifactorial brain metabolic diseases. *Neurobiol Dis*. 2020;143:105014.
59. Edvardson S, et al. Deficiency of the alkaline ceramidase ACER3 manifests in early childhood by progressive leukodystrophy. *J Med Genet*. 2016;53(6):389–396.
60. Bhuiyan RH, et al. Loss of enzyme activity in mutated B4GALNT1 gene products in patients with hereditary spastic paraplegia results in relatively mild neurological disorders: similarity with phenotypes of b4galnt1 knockout mice. *Neuroscience*. 2019;397:94–106.
61. Boccuto L, et al. A mutation in a ganglioside biosynthetic enzyme, ST3GAL5, results in salt & pepper syndrome, a neurocutaneous disorder with altered glycolipid and glycoprotein glycosylation. *Hum Mol Genet*. 2014;23(2):418–433.
62. Harlalka GV, et al. Mutations in B4GALNT1 (GM2 synthase) underlie a new disorder of ganglioside biosynthesis. *Brain*. 2013;136(pt 12):3618–3624.
63. Simpson EP, et al. Increased lipid peroxidation in sera of ALS patients: a potential biomarker of disease burden. *Neurology*. 2004;62(10):1758–1765.
64. Wakil SM, et al. Novel B4GALNT1 mutations in a complicated form of hereditary spastic paraplegia. *Clin Genet*. 2014;86(5):500–501.
65. Wang H, et al. Early growth and development impairments in patients with ganglioside GM3 synthase deficiency. *Clin Genet*. 2016;89(5):625–629.
66. Grob JJ, et al. [Piezogenic cellulo-adipose hernia of the leg]. *Ann Dermatol Venereol*. 1987;114(12):1567–1569.
67. Lone MA, et al. SPTLC1 variants associated with ALS produce distinct sphingolipid signatures through impaired interaction with ORMDL proteins. *J Clin Invest*. 2022;132(18):e161908.
68. Mohassel P, et al. Childhood amyotrophic lateral sclerosis caused by excess sphingolipid synthesis. *Nat Med*. 2021;27(7):1197–1204.
69. Srivastava S, et al. SPTSSA variants alter sphingolipid synthesis and cause a complex hereditary spastic paraplegia. *Brain*. 2023;146(4):1420–1425.
70. Kawano M, et al. Efficient trafficking of ceramide from the endoplasmic reticulum to the Golgi apparatus requires a VAMP-associated protein-interacting FFAT motif of CERT. *J Biol Chem*. 2006;281(40):30279–30288.
71. Firth HV, et al. DECIPHER: database of chromosomal imbalance and phenotype in humans using ensembl resources. *Am J Hum Genet*. 2009;84(4):524–533.
72. Sobreira N, et al. GeneMatcher: a matching tool for connecting investigators with an interest in the same gene. *Hum Mutat*. 2015;36(10):928–930.
73. Richards S, et al. Standards and guidelines for the interpretation of sequence variants: a joint consensus recommendation of the American College of Medical Genetics and Genomics and the Association for Molecular Pathology. *Genet Med*. 2015;17(5):405–424.
74. Karczewski KJ, et al. The mutational constraint spectrum quantified from variation in 141,456 humans. *Nature*. 2020;581(7809):434–443.
75. Wang K, et al. ANNOVAR: functional annotation of genetic variants from high-throughput sequencing data. *Nucleic Acids Res*. 2010;38(16):e164.
76. Jagadeesh KA, et al. M-CAP eliminates a majority of variants of uncertain significance in clinical exomes at high sensitivity. *Nat Genet*. 2016;48(12):1581–1586.
77. Ioannidis NM, et al. REVEL: an ensemble method for predicting the pathogenicity of rare missense variants. *Am J Hum Genet*. 2016;99(4):877–885.
78. Ionita-Laza I, et al. A spectral approach integrating functional genomic annotations for coding and noncoding variants. *Nat Genet*. 2016;48(2):214–220.
79. Lelieveld SH, et al. Spatial clustering of de novo missense mutations identifies candidate neurodevelopmental disorder-associated genes. *Am J Hum Genet*. 2017;101(3):478–484.
80. Schindelin J, et al. Fiji: an open-source platform for biological-image analysis. *Nat Methods*. 2012;9(7):676–682.